Electronic Supplementary Material (ESI) for Nanoscale.
This journal is © The Royal Society of Chemistry 2020

Electronic Supporting Information

Spectral Characterization of $LiYbF_4$ Upconverting Nanoparticles

A. Skripka[1], T. Cheng[1], C. M. S. Jones[2], R. Marin[1,3], J. Marques-Hueso[2] and F. Vetrone[1*]

[1] Institut National de la Recherche Scientifique, Centre Énergie Matériaux Télécommunication, Université du Québec, 1650 Boul. Lionel-Boulet, Varennes, Québec J3X 1S2, Canada.

[2] Institute of Sensors, Signals and Systems, Heriot-Watt University, Edinburgh, EH14 4AS, UK

[3] Fluorescence Imaging Group (FIG), Departamento de Física de Materiales, Facultad de Ciencias, Universidad Autónoma de Madrid, C/ Francisco Tomás y Valiente 7, Madrid 28049, Spain.

***Corresponding author:** vetrone@emt.inrs.ca

Table of Contents

Materials and Methods

Materials

Tm_2O_3 (REacton, 99.997%), Er_2O_3 (REacton, 99.99%), Ho_2O_3 (REacton, 99.997%), Yb_2O_3 (REacton, 99.998%), Y_2O_3 (REacton, 99.999%), trifluoroacetic acid (99%), 1-octadecene (ODE, 90%), oleic acid (OA, 90%), lithium trifluoroacetate (97%) were purchased from Alfa Aesar (USA). Oleylamine (OM, 70%) was obtained from Sigma-Aldrich (USA). All chemicals were used without further purification.

Precursor preparation

Rare-earth (RE) trifluoroacetate precursors (2.5 mmol) for the synthesis of $LiYbF_4:RE^{3+}$ core rare-earth nanoparticles (RENPs) of different RE^{3+} doping (Tm^{3+} - 0.2, 0.5, 1, 2 mol%; Er^{3+} - 1, 2, 5, 10 mol%; Ho^{3+} - 1, 2, 5 mol%) were prepared by mixing stoichiometric quantities of respective RE_2O_3 and Yb_2O_3 (total amount of oxides corresponding to 1.25 mmol) in each case with 5 mL trifluoroacetic acid and 5 mL of water in 50 mL three-neck round bottom flasks. The mixtures were refluxed under vigorous stirring at 80 ºC until the solutions became clear, at which point the temperature was decreased to 60 ºC for residual trifluoroacetic acid and water to evaporate. Yttrium trifluoroacetate precursors for subsequent $LiYF_4$ shelling were prepared in analogous fashion out of Y_2O_3.

RENP synthesis

RENPs were prepared via two-step thermal decomposition method, synthesizing first nuclei (FN) which serve as seeds to form the desired core RENPs.[1]

FN formation: An initial mixture of 7 mL each of OA and OM, and 14 mL of ODE, was prepared in a 100 mL three-neck round bottom flask (Solution A). Solution A was degassed under vacuum at 110 ºC for 15 min, after which it was back-filled with Ar and the temperature was raised to 330 ºC. Meanwhile, 2.5 mmol of lithium trifluoroacetate was added to the dried core precursors together with 3 mL of OA and 6 mL of ODE (Solution B). Solution B was then degassed under vacuum at 125 ºC for 30 min. 3 mL of OM were added in Solution B after precursors were completely dissolved, and left to degas under stirring for additional 5 min. Once Solution A reached stable temperature, Solution B was injected into Solution A using a pump-syringe system (Harvard Apparatus Pump 11 Elite, USA) with injection rate of 1.5 mL/min. After 1 h of vigorous stirring at 330 ºC, the mixture was cooled down to room temperature. The synthesized FN were stored in Falcon centrifuge tubes (50 mL) under Ar for the subsequent stabilization step. Due to evaporation of impurities in the starting materials (such as OA and ODE) and reaction byproducts, as well as minor losses accrued from intermediate steps of liquid handling, the final volume of FN mixtures was around 36-37 mL.

Core synthesis: Core RENPs were formed by the stabilization of FN with excess of OA. Note, at room temperature the FN mixture is solid, and was liquefied by heating up the solution inside the Falcon tube in warm water prior to the synthesis. FN (1.25 mmol, ~ 18-18.5 mL of stock solution) was mixed with 16 mL each of OA and ODE in a 100 mL three-neck round bottom flask. The solution was degassed at 110 ºC under vacuum and magnetic stirring for 30 min. Then, back-filled with Ar and the temperature was raised to 315 ºC, at which point the reaction continued for 1 h. After cooling to RT, a small portion (1 mL) of core RENPs was sampled for characterization.

Core shelling: Core/shell RENPs were prepared by epitaxial growth of the shell on the preformed cores via the hot-injection approach. Approximately 0.5 mmol of core RENPs were mixed in 100 mL three-neck round bottom flask together with equal parts of OA and ODE up to a total volume of 20 mL (Solution A). Separately, Solution B was prepared by mixing 4 mmol of yttrium trifluoroacetate precursors together with 4 mmol of lithium trifluoroacetate, and 10 mL each of OA and ODE. Both solutions were degassed under vacuum and magnetic stirring at 110 ºC for 30 min. After degassing, Solution A was back-filled with Ar and the temperature was raised to 290 ºC. Solution B was then injected into the reaction vessel containing Solution A using a syringe and pump system at a 0.75 mL/min injection rate in three steps. After each ~ 7 mL injection step, the mixture was allowed to react for 40 min. After the last reaction step, the mixture was cooled to RT under Ar and magnetic stirring. Resultant core/shell RENPs were precipitated with ethanol and washed three times with hexane/acetone (1/4 v/v in each case), followed by centrifugation (5400 RCF). Finally, RENPs were re-dispersed in hexane for further structural and optical characterization.

Structural characterization

The crystallinity and phase of the core and core/shell RENPs were determined via X-ray powder diffraction (XRD) analysis with a Bruker D8 Advance Diffractometer (USA) using CuKα radiation. The morphology and size distribution of the core-only and core/shell RENPs were investigated by transmission electron microscopy (TEM, Philips Tecnai 12, USA). The particle size was determined from TEM images using ImageJ image analysis software with set size of at least 200 individual particles per sample. RE^{3+} molar doping concentration was determined via inductively coupled plasma - optical emission spectroscopy (ICP-OES) with an Agilent Technologies 5100 ICP-OES spectrometer (USA).

Optical characterization

Upconversion emission spectra of 5 wt% hexane dispersions of RENPs were obtained at room temperature under 960 nm continuous-wave laser diode excitation (BWT, China). Laser beam area on target was 0.000615 cm^2. The upconversion emission was collected using a lens at a 90º angle from the excitation beam and recorded with an Avaspec-ULS2048L spectrometer (Avantes, The Netherlands). Nominal spectral resolution of the spectrometer is 2.4 nm. Acquired data was spectrally corrected using black body emission approximation, and further normalized for difference in photon energies across measured spectral range. Stray light from the excitation source was removed with short-pass 825 nm filter (Newport Corp., USA). The downshifting emission spectra of RENPs in the NIR region was collected with a Shamrock 500i monochromator (Andor, Ireland) equipped with an iDus InGaAs 1.7 NIR detector (Andor, Ireland). In order to remove any stray light from the excitation source, a long-pass 980 nm filter was used. Laser excitation power density was ~30 W/cm^2.

Upconversion photoluminescence lifetime measurements were performed on a FLS980 (Edinburgh Instruments Ltd., UK) spectrometer equipped with a double emission monochromator, single-photon counting photomultiplier (Hamamatsu R928, Japan), and a 1 W 980 nm pulsed laser diode MDL-III-980 (CNI, China) with 70 µs pulse width and 100 Hz repetition rate. Average decay (and rise) time values were obtained from integrated area under the decay (rise) profiles:

$$\tau = \int_{t_1}^{t_2} \frac{I(t)dt}{I(0)}$$

Integration range t_1 and t_2 was from 0 to +∞ for decay time evaluation, and from -∞ to 0 for rise time.

A calibrated spectrometer FLS920 (Edinburgh Instruments Ltd., UK), equipped with a double emission monochromator, was used to determine the absolute upconversion quantum yield (*UCQY*). Each sample was transferred to an optical cuvette of ~0.6 cm optical path, placed inside an integrating sphere (Jobin-Yvon), and excited using a 10 W 960 nm continuous-wave laser diode (BWT, Beijing). Laser beam area on target was 0.000434 cm^2. The emission was measured using an extended red-sensitive single-photon counting photomultiplier detector (Hamamatsu, PMT, 200-1010 nm). The emission monochromator bandwidth was kept constant for each emission and related absorption measurement. However, it varied from 2 to 5 nm, depending on excitation power, to avoid saturation of the detector (lower bandwidth values for higher excitation powers). Excitation power density was varied by placing different optical density (OD) filters in the excitation path. A 610 nm long-pass filter was used over the 600-850 nm range to avoid second order emission artifacts when measuring Tm^{3+}-RENPs. Marginal-filter-induced photon loss was later corrected for. The emitted photon number was calculated from the emission spectra of each RENP sample. The absorbed photons were found by subtracting the incident beam intensity on the RENPs sample from the incident beam intensity on a reference sample of pure hexane, with identical volume. By dividing the total number of emitted photons (over the range 310-850 nm) by the total number of absorbed photons at 960 nm, the *UCQY* was determined for each sample over a variety of powers. All spectra were corrected by the system response. All *UCQY* values have ±10% relative error.

Relative spectral contribution (I_λ/I_{total}) and *UCQY* data were calculated from integrated intensity values of specific emission bands (I_λ) and total emission (I_{total}). Tm^{3+}-RENPs: 332-358 ($^1I_6 \rightarrow {}^3F_4$), 358-373 ($^1D_2 \rightarrow {}^3H_6$), 433-461 ($^1D_2 \rightarrow {}^3F_4$), 461-502 ($^1G_4 \rightarrow {}^3H_6$), 609-692 ($^1G_4 \rightarrow {}^3F_4$) and 697-830 nm ($^3H_4 \rightarrow {}^3H_6/{}^1G_4 \rightarrow {}^3H_5$; in the case of *UCQY* measurements no NIR band deconvolution was used). Er^{3+}-RENPs: 374-392 ($^4G_{11/2} \rightarrow {}^4I_{15/2}$), 396-428 ($^2H_{9/2} \rightarrow {}^4I_{15/2}$), 511-581 ($^2H_{11/2}/^4S_{3/2} \rightarrow {}^4I_{15/2}$) and 625-713 nm ($^4F_{9/2} \rightarrow {}^4I_{15/2}$). Ho^{3+}-RENPs: 468-503 ($^5F_3 \rightarrow {}^5I_8$), 513-569 ($^5S_2/^5F_4 \rightarrow {}^5I_8$), 614-693 ($^5F_5 \rightarrow {}^5I_8$) and 736-763 nm ($^5S_2/^5F_4 \rightarrow {}^5I_7$). For the *UCQY* measurements laser line intensity was integrated over 952-967 nm range.

TEM images and size distribution of $LiYbF_4$:RE^{3+}/$LiYF_4$ RENPs

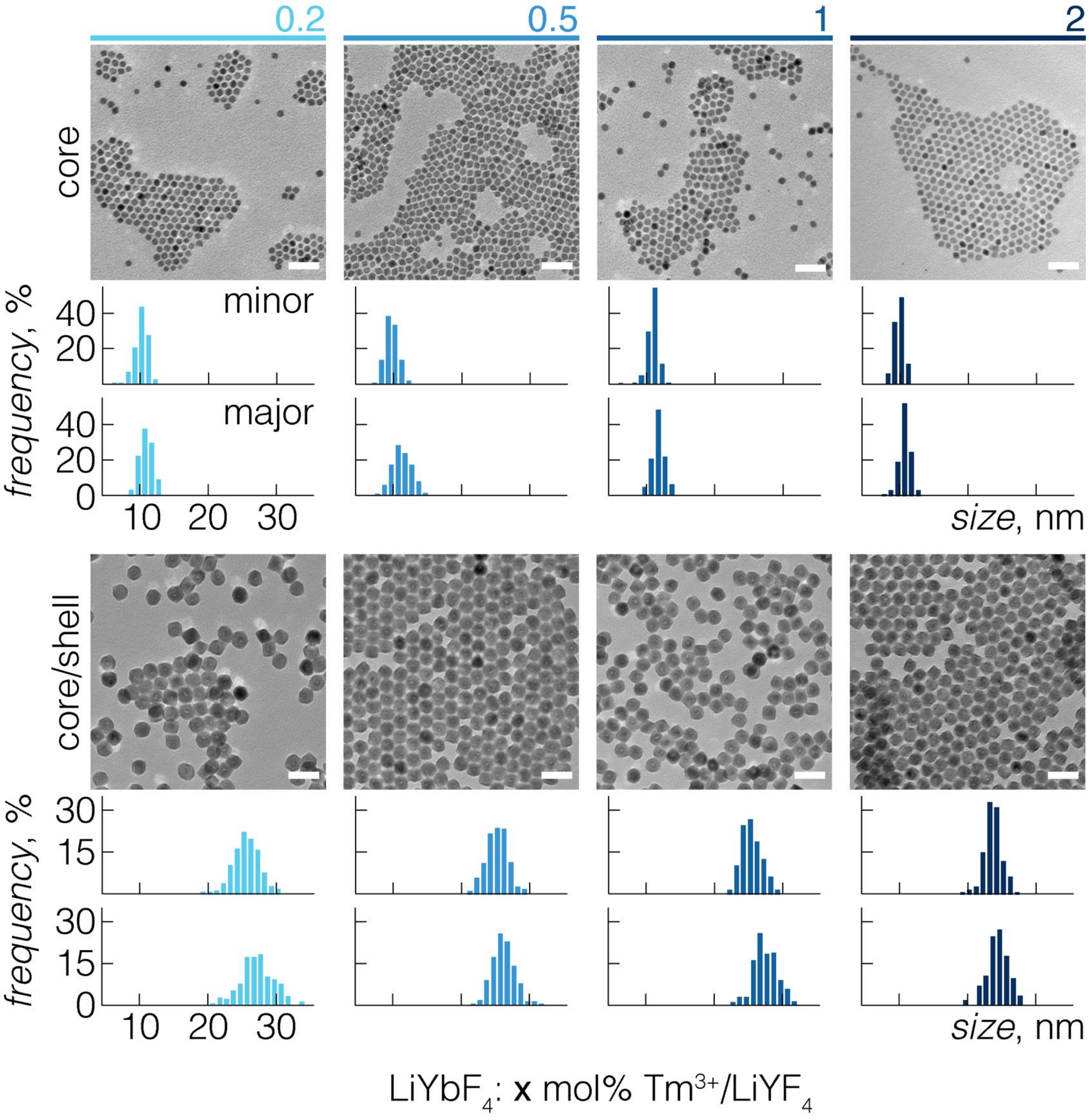

Figure S1. TEM images of $LiYbF_4$: x mol% Tm^{3+} – core and core/$LiYF_4$ – shell RENPs. Their respective size distributions were measured along major (lower plot) and minor (upper plot) axes of an elliptical fit.

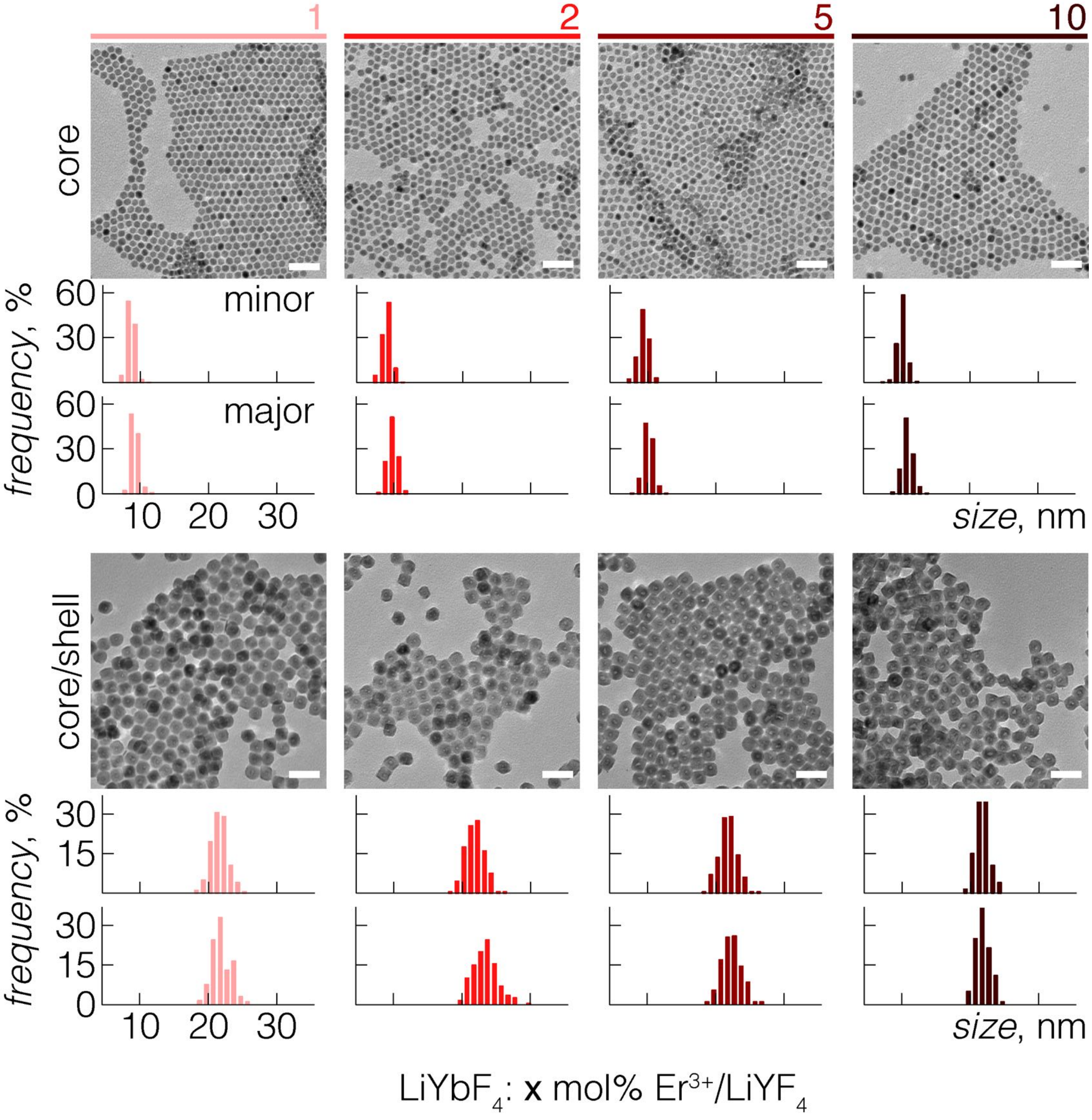

Figure S2. TEM images of LiYbF$_4$: x mol% Er^{3+} – core and core/LiYF$_4$ – shell RENPs. Their respective size distributions were measured along major (lower plot) and minor (upper plot) axes of an elliptical fit.

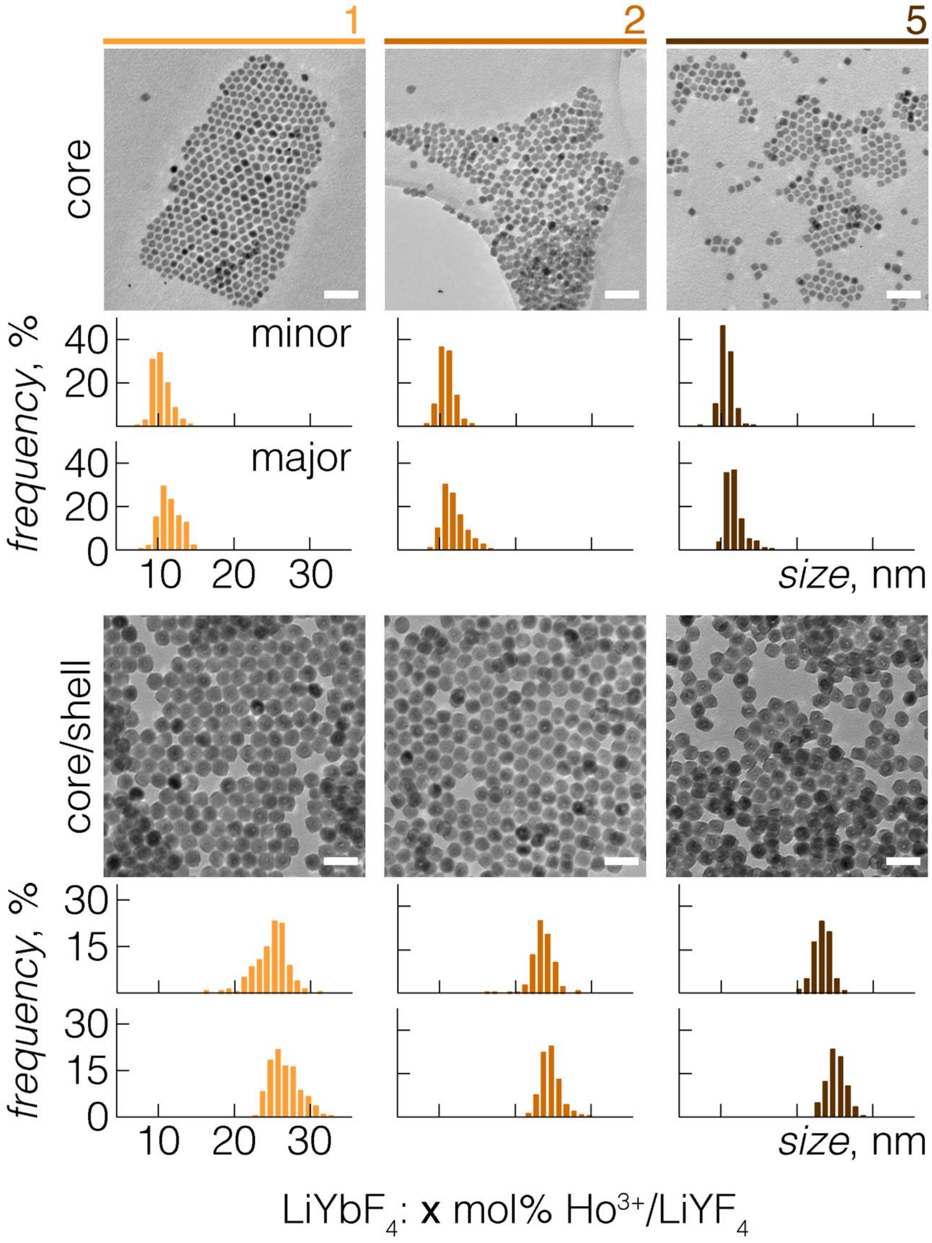

Figure S3. TEM images of $LiYbF_4$: x mol% Ho^{3+} – core and core/$LiYF_4$ – shell RENPs. Their respective size distributions were measured along major (lower plot) and minor (upper plot) axes of an elliptical fit.

XRD patterns of LiYbF$_4$:RE^{3+}/LiYF$_4$ RENPs

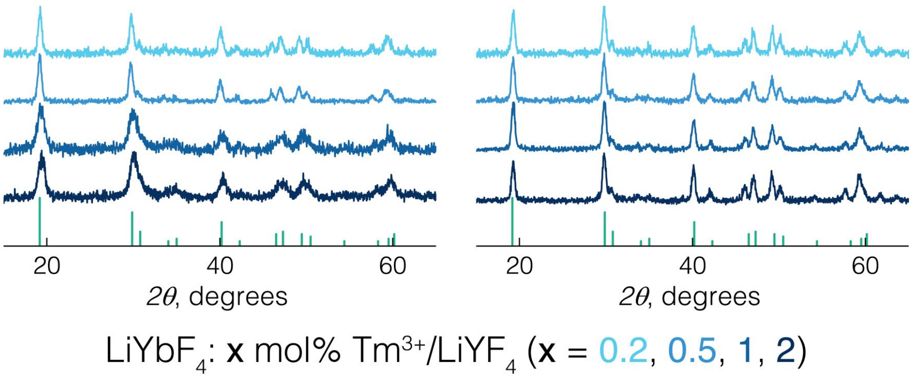

Figure S4. XRD patterns of LiYbF$_4$: x mol% Tm^{3+} – core (left) and core/LiYF$_4$ – shell (right) RENPs. Diffraction peaks of pure tetragonal LiYbF$_4$ are shown in green (PDF# 00-023-0371).

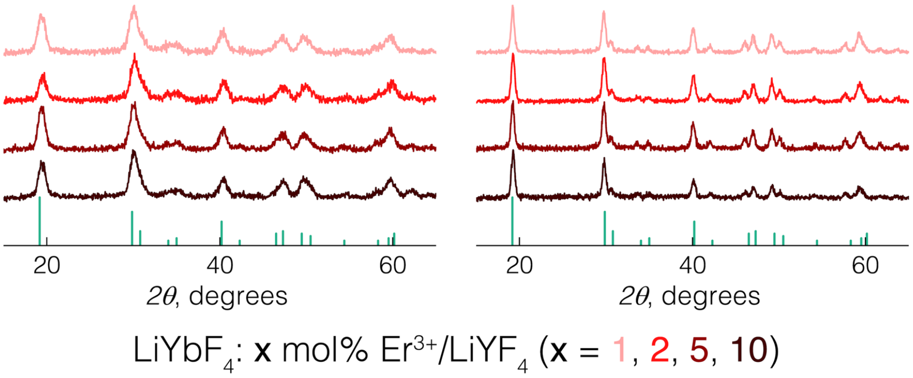

Figure S5. XRD patterns of LiYbF$_4$: x mol% Er^{3+} – core and core/LiYF$_4$ – shell RENPs. Diffraction peaks of pure tetragonal LiYbF$_4$ are shown in green (PDF# 00-023-0371).

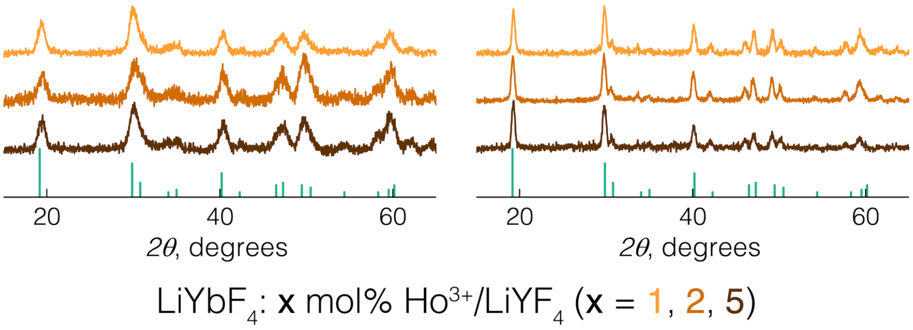

Figure S6. XRD patterns of LiYbF$_4$: x mol% Ho^{3+} – core and core/LiYF$_4$ – shell RENPs. Diffraction peaks of pure tetragonal LiYbF$_4$ are shown in green (PDF# 00-023-0371).

Summary of structural and morphological properties of LiYbF$_4$:RE^{3+}/LiYF$_4$ RENPs

Table S1. Overview of structural and morphological characteristics of LiYbF$_4$:RE^{3+}/LiYF$_4$ RENPs: nominal and actual doping in mol% (measured via ICP-OES with maximum relative error of 15%), core and core/shell size of RENPs measured along their major and minor axes, and respective estimate of shell thickness.

RE^{3+} doping (nominal), mol%	RE^{3+} doping (actual), mol%	core size, nm		core/shell size, nm		shell thickness, nm
		major	minor	major	minor	
LiYbF$_4$:Tm^{3+}/LiYF$_4$						
0.2	**0.22**	**11.2±0.9**	**11.0±0.9**	**27.5±2.4**	**25.4±1.8**	**~8.2 x 7.7**
0.5	**0.51**	**11.5±1.3**	**9.5±0.9**	**26.4±1.6**	**25.0±1.5**	**~7.5 x 7.8**
1	**1.03**	**12.0±0.8**	**10.7±0.7**	**27.8±1.7**	**25.2±1.4**	**~7.9 x 7.3**
2	**2.09**	**11.0±0.8**	**9.7±0.7**	**24.8±1.5**	**23.5±1.2**	**~6.9 x 6.9**
LiYbF$_4$:Er^{3+}/LiYF$_4$						
1	**1.06**	**9.5±0.6**	**8.4±0.5**	**22.2±1.3**	**21.3±1.2**	**~6.4 x 6.5**
2	**1.83**	**10.1±0.7**	**8.7±0.7**	**23.7±1.8**	**21.6±1.3**	**~6.8 x 6.5**
5	**4.89**	**10.4±0.7**	**9.1±0.7**	**22.6±1.4**	**21.5±1.4**	**~6.1 x 6.2**
10	**9.96**	**11.2±0.8**	**9.8±0.6**	**22.1±1.1**	**21.5±1.0**	**~5.5 x 5.9**
LiYbF$_4$:Ho^{3+}/LiYF$_4$						
1	**1.32**	**11.8±1.4**	**10.1±1.2**	**27.1±2.5**	**24.6±2.1**	**~7.7 x 7.3**
2	**2.02**	**12.1±1.5**	**10.6±1.1**	**24.9±1.5**	**23.4±1.4**	**~6.4 x 6.4**
5	**5.34**	**12.0±1.2**	**10.5±0.8**	**25.4±1.2**	**23.0±1.1**	**~6.7 x 6.3**

Spectral deconvolution of Tm^{3+}-RENPs NIR PL

Spectra of NIR emission of Tm^{3+}-RENPs around 790 nm ($y_{obs,i}$) were fitted point by point via linear combination of the spectral profiles of the (y_i) of $^3H_4 \rightarrow {}^3H_6$ (Q_i) and $^1G_4 \rightarrow {}^3H_5$ (U_i) transitions (Figure S7). Given that the $^3H_4$ excited state quickly saturates for 0.2 mol% Tm^{3+}-doped RENPs at higher power density (P_d), its 790 nm emission at P_d > 2k W/cm^2 was considered as the closest representation of pristine $^1G_4 \rightarrow {}^3H_5$ radiative transition. In contrast, 2 mol% Tm^{3+}-doped RENPs prominently featured 790 nm PL from the $^3H_4 \rightarrow {}^3H_6$ radiative transition, which for purity was measured at P_d < 5 W/cm^2. The mathematical procedure then relies on the minimization of a squared residual function S:

$$S = \sum_i (y_{obs,i} - y_i)^2 = \sum_i [y_{obs,i} - (aQ_i + bU_i)]^2$$

a and *b* are weighing coefficients that account for the contribution of each radiative transition.

Imposing the first order derivative of this function, calculated with respect to the weighing coefficients, to be equal to zero minimizes S:

$$\frac{\partial S}{\partial a} = \frac{\partial S}{\partial b} = 0$$

This leads to the homogeneous system:

$$\begin{pmatrix} \sum_i Q_i^2 & \sum_i Q_i U_i \\ \sum_i U_i Q_i & \sum_i U_i^2 \end{pmatrix} \begin{pmatrix} a \\ b \end{pmatrix} = \begin{pmatrix} \sum_i Q_i y_{obs,i} \\ \sum_i U_i y_{obs,i} \end{pmatrix}$$

And, rearranged:

$$\begin{pmatrix} a \\ b \end{pmatrix} = \begin{pmatrix} \sum_i Q_i^2 & \sum_i Q_i U_i \\ \sum_i U_i Q_i & \sum_i U_i^2 \end{pmatrix}^{-1} \begin{pmatrix} \sum_i Q_i y_{obs,i} \\ \sum_i U_i y_{obs,i} \end{pmatrix}$$

By solving this system, the values *a* and *b* are obtained, thus the relative contribution to the total Tm^{3+} PL at 790 nm from the two radiative transitions can be extracted.

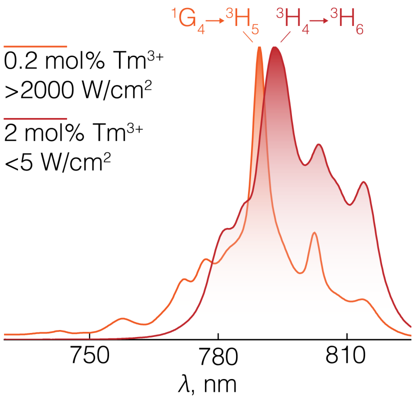

Figure S7. Emission profiles used for spectral deconvolution of the NIR band around 790 nm measured for 0.2 mol% and 2 mol% Tm^{3+}-RENPs under high and low P_d of 960 nm laser excitation, respectively. The former RENPs represent the $^1G_4 \rightarrow {}^3H_5$ radiative transition while the latter represents the $^3H_4 \rightarrow {}^3H_6$ one.

Intensity interplay of Tm^{3+}-RENPs PL bands

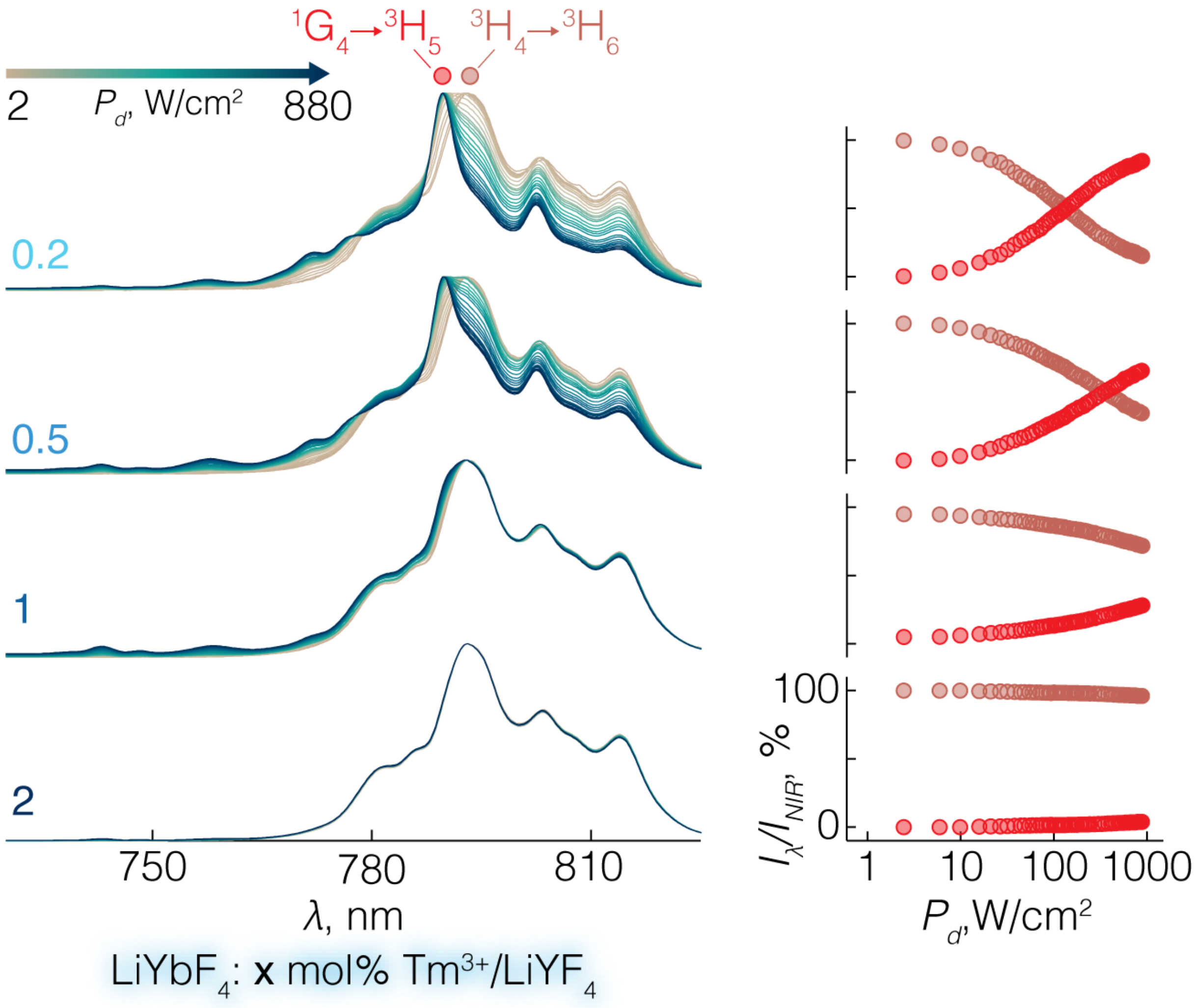

Figure S8. Normalized NIR PL spectra of $LiYbF_4$: x mol% $Tm^{3+}/LiYF_4$ RENPs under 960 nm laser excitation of varied P_d (left). Relative contributions of $^3H_4 \rightarrow {}^3H_6$ and $^1G_4 \rightarrow {}^3H_5$ radiative transitions to the total NIR PL of Tm^{3+}-RENPs (right).

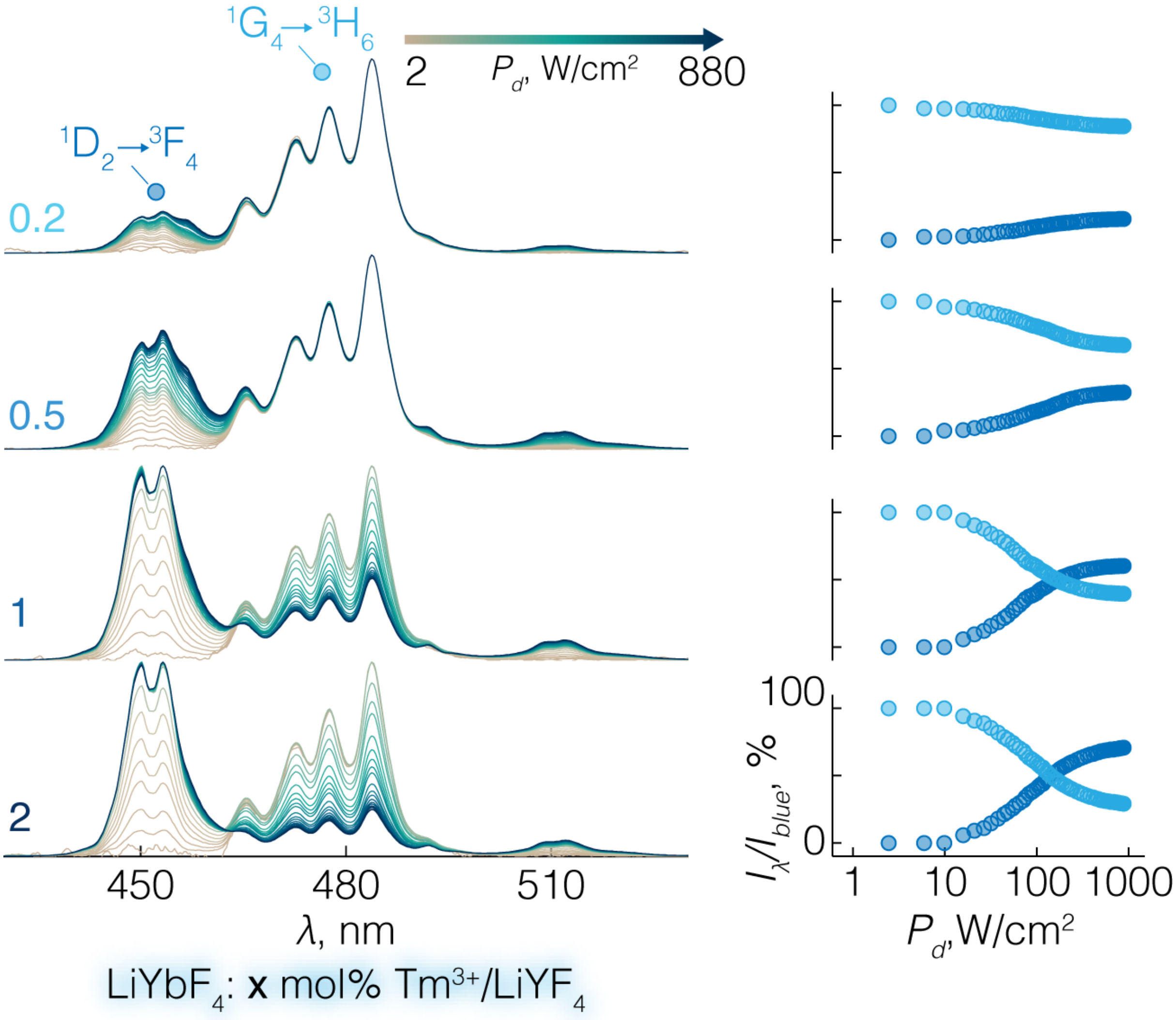

Figure S9. Normalized blue PL spectra of LiYbF$_4$: x mol% Tm^{3+}/LiYF$_4$ RENPs under 960 nm laser excitation of varied P_d (left). Relative contributions of $^1D_2 \rightarrow {}^3F_4$ and $^1G_4 \rightarrow {}^3H_6$ radiative transitions to the total blue PL of Tm^{3+}-RENPs (right).

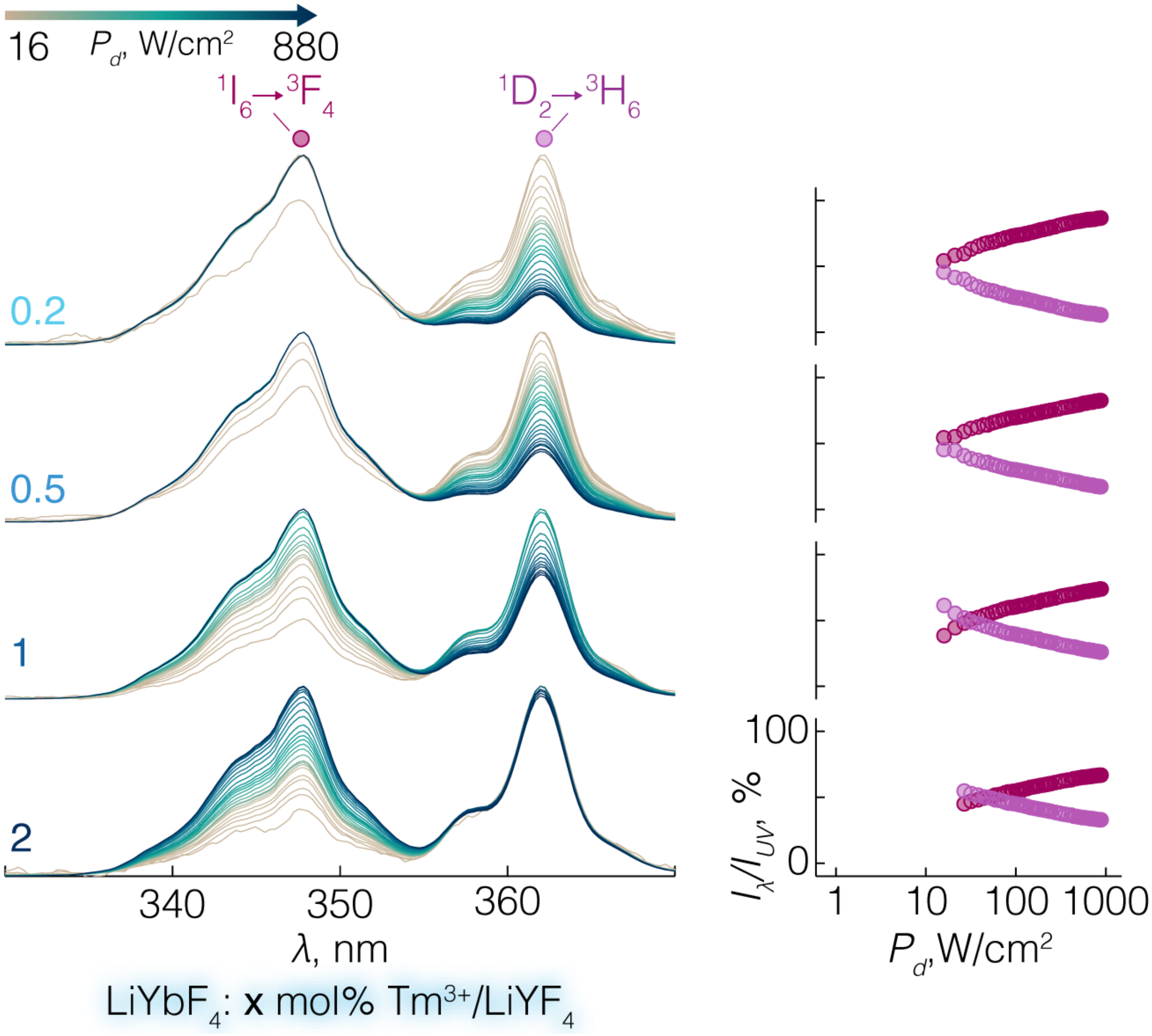

Figure S10. Normalized UV PL spectra of LiYbF$_4$: x mol% Tm^{3+}/LiYF$_4$ RENPs under 960 nm laser excitation of varied P_d (left). Relative contributions of $^1I_6 \rightarrow ^3F_4$ and $^1D_2 \rightarrow ^3H_6$ radiative transitions to the total UV PL of Tm^{3+}-RENPs (right).

Power plots of Tm^{3+}-RENPs PL

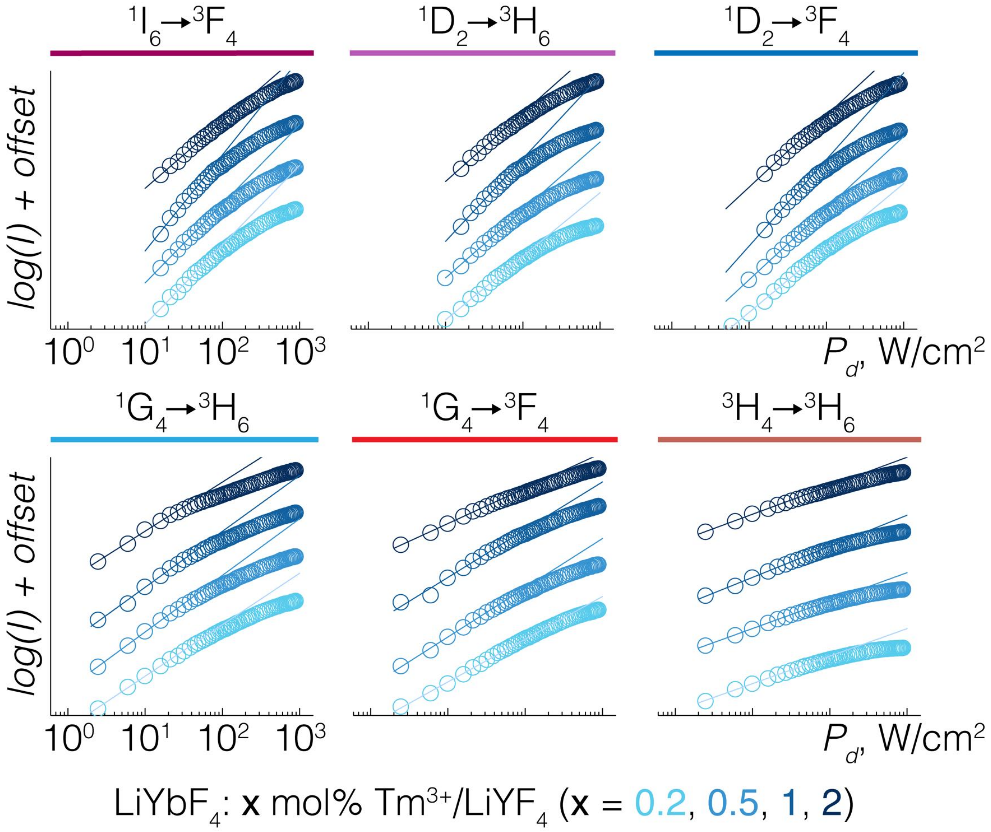

Figure S11. Intensity vs excitation P_d log-log plots of different upconversion PL bands of LiYbF$_4$: x mol% Tm^{3+}/LiYF$_4$ RENPs under 960 nm laser excitation. Linear fits performed for the low P_d regime (2 – 20 W/cm^2; 10 – 40 W/cm^2 for highest order upconversion emissions), slope values are summarized in the table below.

Table S2. Slope values of linear fits in Figure S11.

Transition x mol% Tm^{3+}	**$^1I_6 \rightarrow {}^3F_4$**	**$^1D_2 \rightarrow {}^3H_6$**	**$^1D_2 \rightarrow {}^3F_4$**	**$^1G_4 \rightarrow {}^3H_6$**	**$^1G_4 \rightarrow {}^3F_4$**	**$^3H_4 \rightarrow {}^3H_6$**
0.2	3.60 ± 0.14	2.88 ± 0.10	2.92 ± 0.08	2.53 ± 0.05	2.10 ± 0.06	1.35 ± 0.03
0.5	3.58 ± 0.10	3.08 ± 0.07	3.24 ± 0.09	2.78 ± 0.06	2.42 ± 0.06	1.37 ± 0.02
1	4.35 ± 0.24	3.74 ± 0.19	3.92 ± 0.20	2.75 ± 0.12	2.35 ± 0.19	1.53 ± 0.05
2	3.04 ± 0.13	3.11 ± 0.12	3.25 ± 0.17	2.41 ± 0.08	1.74 ± 0.04	1.40 ± 0.04

Decay and rise profiles of Tm^{3+}-RENPs excited states

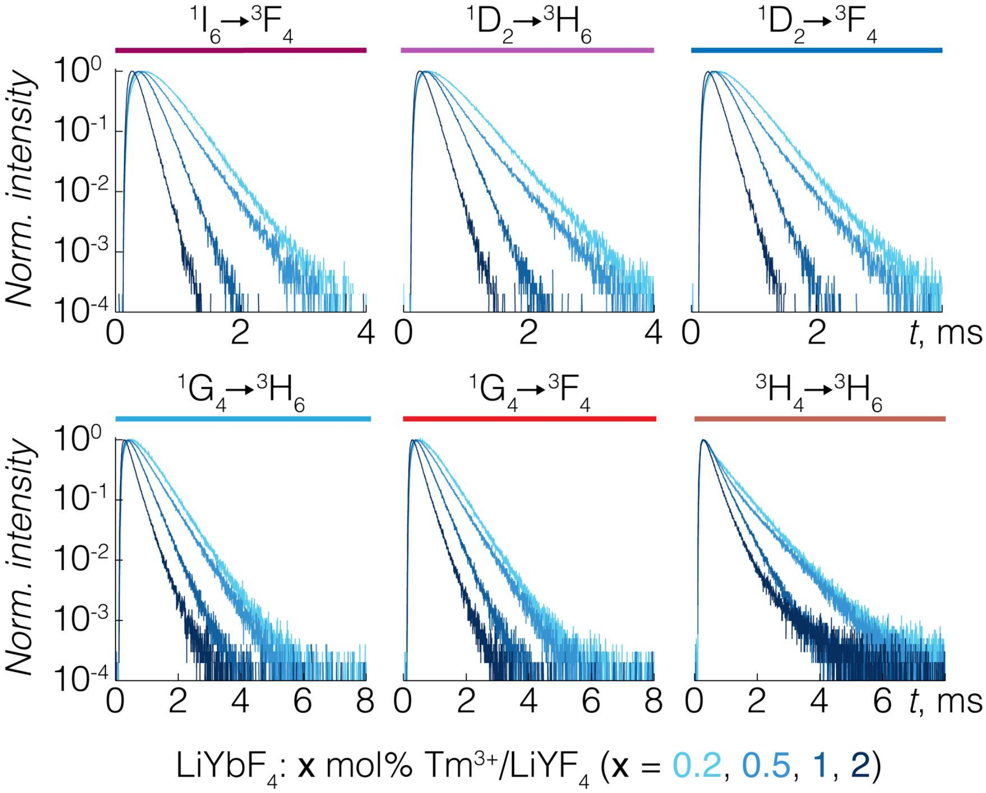

Figure S12. Normalized PL decay profiles of different upconversion emissions of $LiYbF_4$: x mol% $Tm^{3+}/LiYF_4$ RENPs under 980 nm laser excitation. Average decay values, τ, are summarized in Table S3.

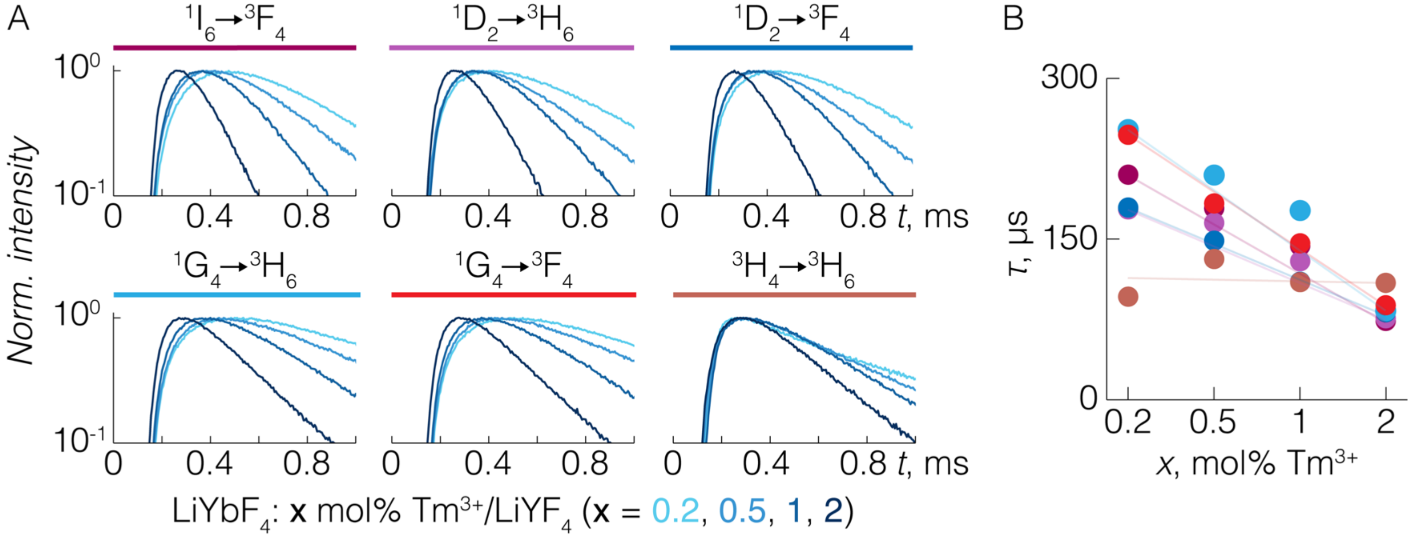

Figure S13. A – Close-up on the PL decay profiles in Figure S12, exemplifying change in the rise times with increasing Tm^{3+} doping concentration in $LiYbF_4$: x mol% $Tm^{3+}/LiYF_4$ RENPs. B - average rise time, τ_r, for different Tm^{3+} excited states as a function of $c(Tm^{3+})$, also summarized in Table S3. Lines in B serve as guides to the eye.

Table S3. Average decay (τ) and rise (τ_r) times (in μs) of different Tm^{3+} excited states in $LiYbF_4$: x mol% Tm^{3+}/$LiYF_4$ RENPs. Values in parenthesis indicate relative change compared to the 0.2 mol% Tm^{3+} doping.

Transition x mol% Tm^{3+}	$^1I_6\rightarrow{}^3F_4$		$^1D_2\rightarrow{}^3H_6$		$^1D_2\rightarrow{}^3F_4$		$^1G_4\rightarrow{}^3H_6$		$^1G_4\rightarrow{}^3F_4$		$^3H_4\rightarrow{}^3H_6$	
	τ	τ_r	τ	τ_r	τ	τ_r	τ	τ_r	τ	τ_r	τ	τ_r
0.2	478	210	549	177	530	179	761	252	755	247	778	96
0.5	386 (-19%)	179 (-15%)	404 (-26%)	165 (-7%)	415 (-21%)	148 (-17%)	629 (-17%)	210 (-16%)	660 (-13%)	183 (-26%)	586 (-25%)	131 (+36%)
1	262 (-45%)	143 (-32%)	315 (-43%)	129 (-27%)	320 (-40%)	110 (-39%)	428 (-44%)	177 (-30%)	454 (-40%)	146 (-41%)	477 (-39%)	110 (+15%)
2	176 (-63%)	74 (-65%)	195 (-64%)	76 (-66%)	178 (-66%)	81 (-55%)	313 (-59%)	83 (-67%)	307 (-59%)	88 (-64%)	340 (-56%)	109 (+14%)

Green to red PL intensity ratio of Er^{3+}-RENPs

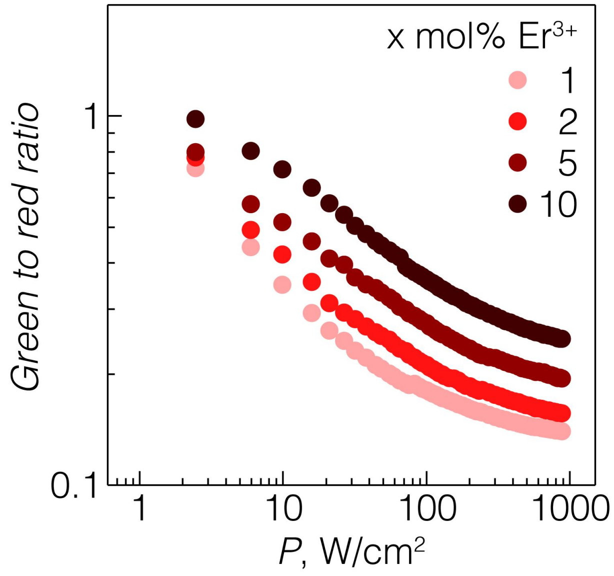

Figure S14. Green to red upconversion emission ratio of LiYbF$_4$: x mol% Er^{3+}/LiYF$_4$ RENPs under 960 nm laser excitation of different P_d.

Power plots of Er^{3+}-RENPs PL

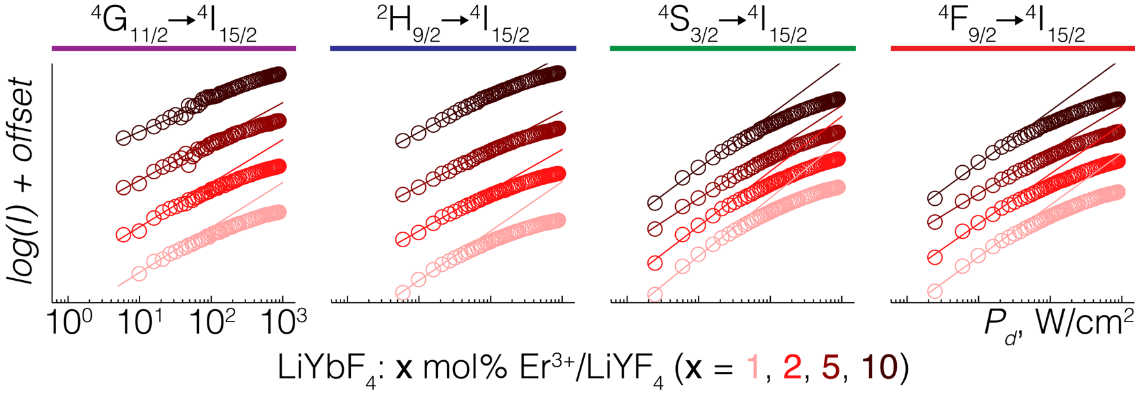

Figure S15. Intensity vs excitation P_d log-log plots of different upconversion PL bands of LiYbF$_4$: x mol% Er^{3+}/LiYF$_4$ RENPs under 960 nm laser excitation. Linear fits performed for the low P_d regime (2 – 20 W/cm^2), slope values are summarized in the table below.

Table S4. Slope values of linear fits in Figure S15.

Transition x mol% Er^{3+}	**$^4G_{11/2}\rightarrow{}^4I_{15/2}$**	**$^2H_{9/2}\rightarrow{}^4I_{15/2}$**	**$^4S_{3/2}\rightarrow{}^4I_{15/2}$**	**$^4F_{9/2}\rightarrow{}^4I_{15/2}$**
1	2.20 ± 0.27	2.41 ± 0.12	1.73 ± 0.09	2.19 ± 0.11
2	2.13 ± 0.23	1.99 ± 0.10	1.67 ± 0.11	2.07 ± 0.13
5	1.90 ± 0.19	1.83 ± 0.07	1.46 ± 0.07	1.75 ± 0.08
10	1.52 ± 0.10	1.87 ± 0.04	1.76 ± 0.09	2.00 ± 0.09

Decay and rise profiles of Er^{3+}-RENPs excited states

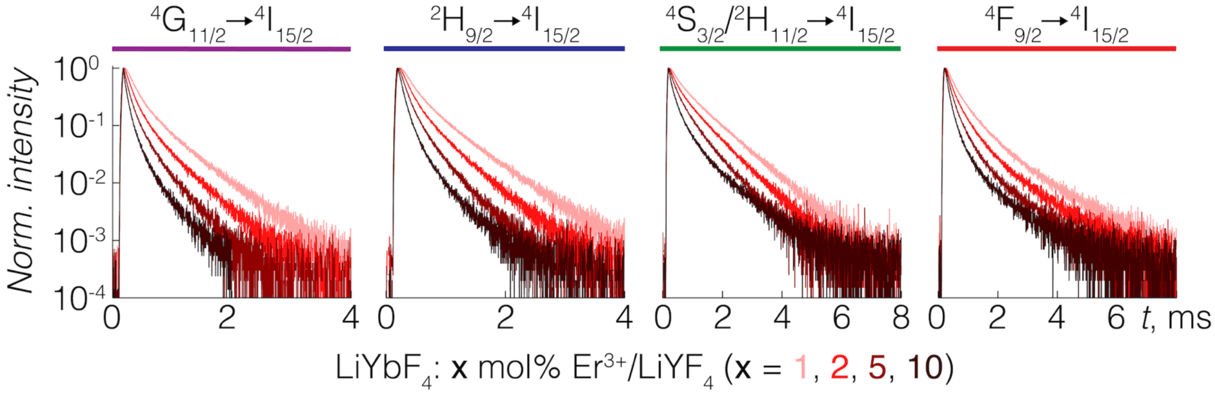

Figure S16. Normalized PL decay profiles of different upconversion emissions of $LiYbF_4$: x mol% $Er^{3+}/LiYF_4$ RENPs under 980 nm laser excitation. Average decay values, τ, are summarized in Table S5.

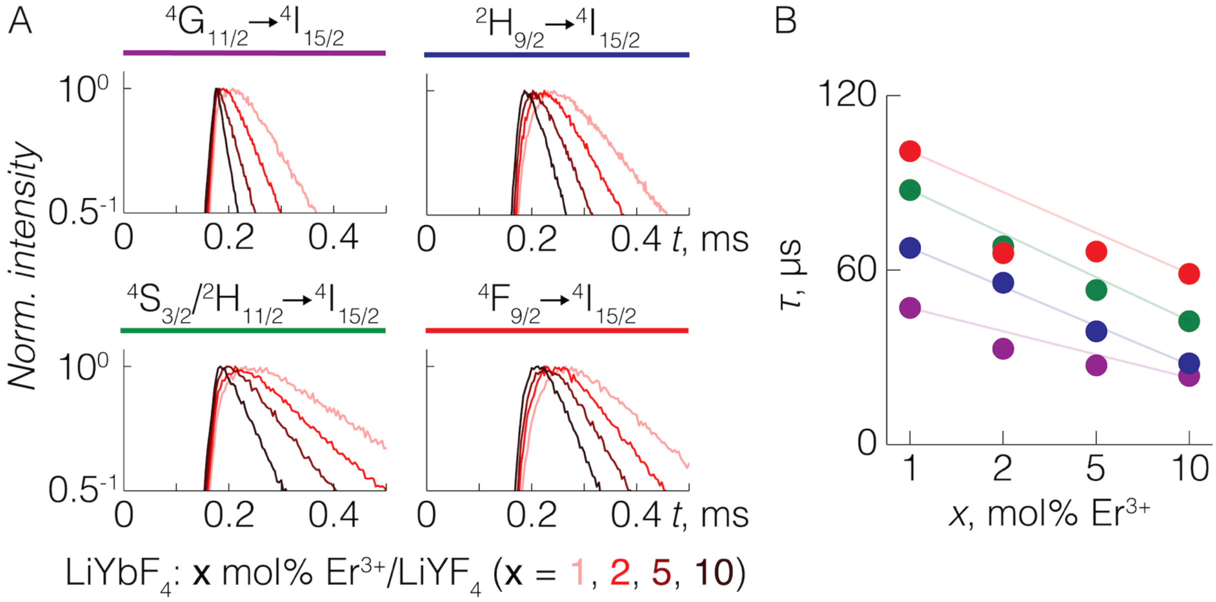

Figure S17. A – Close-up on the PL decay profiles in Figure S16, exemplifying change in the rise times with increasing Er^{3+} doping amount in $LiYbF_4$: x mol% $Er^{3+}/LiYF_4$ RENPs. B - average rise time, τ_r, for different Er^{3+} excited states as a function of $c(Er^{3+})$, also summarized in Table S5. Lines in B serve as guides to the eye.

Table S5. Average decay (τ) and rise (τ_r) times (in μs) of different Er^{3+} excited states in $LiYbF_4$: x mol% Er^{3+}/$LiYF_4$ RENPs. Values in parenthesis indicate relative change compared to the 1 mol% Er^{3+} doping.

Transition / x mol% Er^{3+}	$^4G_{11/2}\rightarrow{}^4I_{15/2}$		$^2H_{9/2}\rightarrow{}^4I_{15/2}$		$^4S_{3/2}\rightarrow{}^4I_{15/2}$		$^4F_{9/2}\rightarrow{}^4I_{15/2}$	
	τ	τ_r	τ	τ_r	τ	τ_r	τ	τ_r
1	278	47	362	68	720	88	530	101
2	193 (-31%)	33 (-30%)	255 (-30%)	56 (-18%)	534 (-26%)	68 (-23%)	402 (-24%)	66 (-35%)
5	127 (-54%)	27 (-43%)	183 (-49%)	39 (-43%)	391 (-46%)	53 (-40%)	286 (-46%)	66 (-35%)
10	81 (-71%)	24 (-49%)	128 (-65%)	28 (-59%)	263 (-63%)	42 (-52%)	204 (-62%)	59 (-42%)

UCQY of Er^{3+}-RENPs

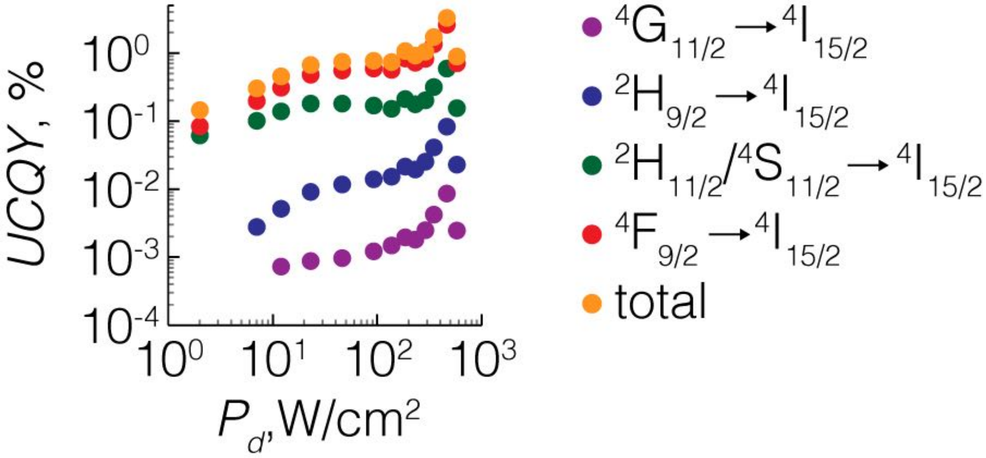

Figure S18. *UCQY* of LiYbF$_4$: 5 mol% Er^{3+}/LiYF$_4$ RENPs vs 960 nm laser excitation P_d, measured for major Er^{3+} upconversion PL bands.

Ho^{3+}-RENPs upconversion PL, close-up

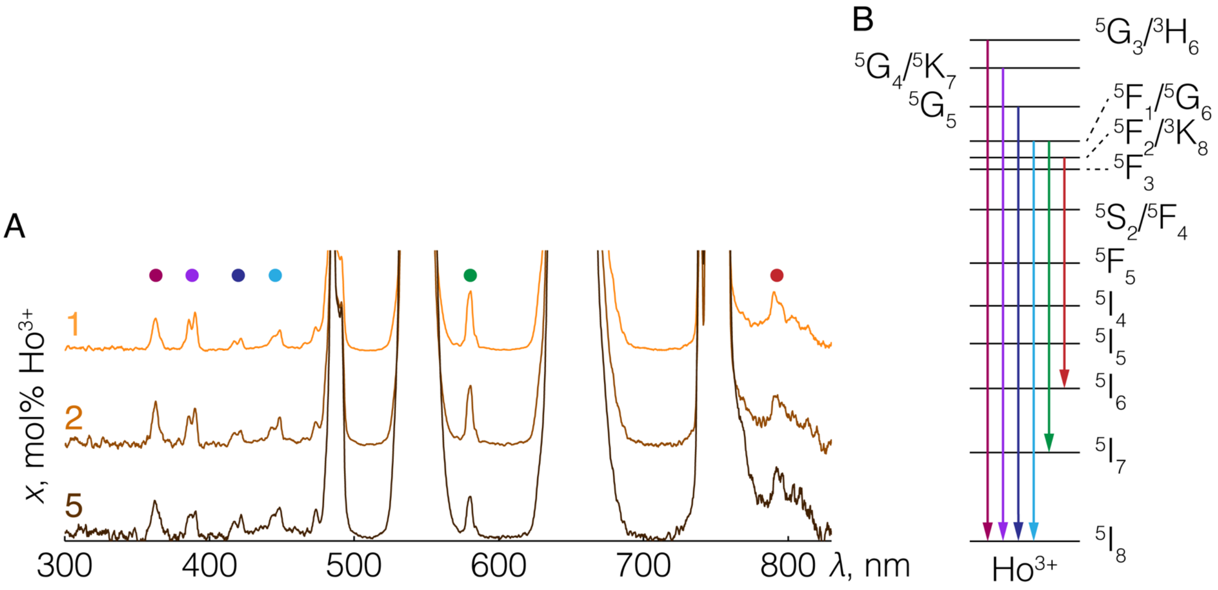

Figure S19. A – Close-up on the upconversion PL spectra of LiYbF$_4$: x mol% Ho^{3+}/LiYF$_4$ RENPs, under 960 nm laser excitation of P_d ~ 200 W/cm^2. B – simplified Ho^{3+} energy level scheme and tentatively assigned (colour-coded) radiative transitions.

Green to red PL intensity ratio of Ho^{3+}-RENPs

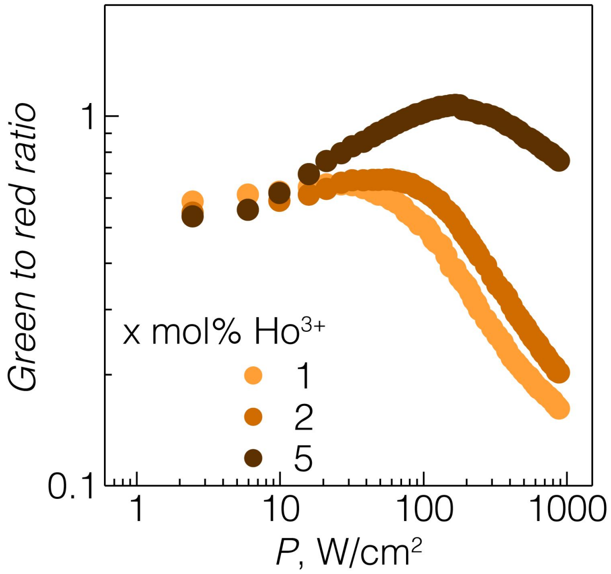

Figure S20. Green to red upconversion emission ratio of $LiYbF_4$: x mol% $Ho^{3+}/LiYF_4$ RENPs under 960 nm laser excitation of different P_d.

Power plots of Ho^{3+}-RENPs PL

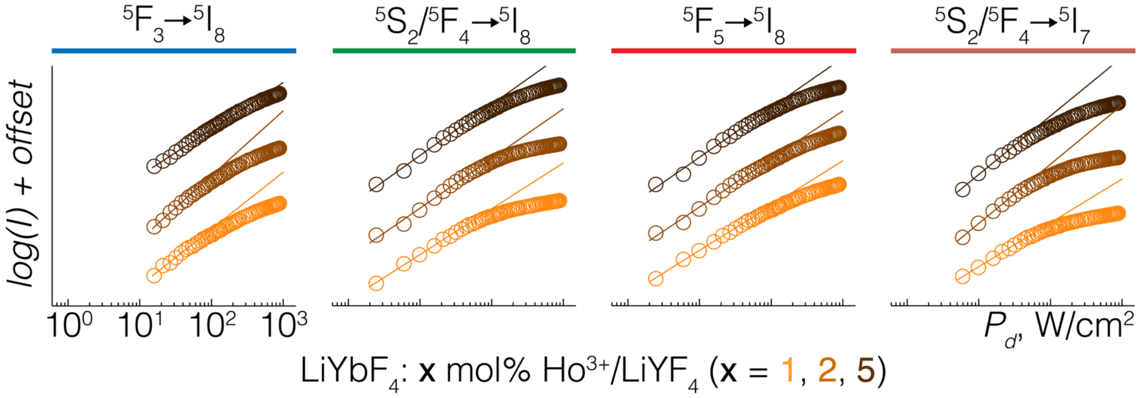

Figure S21. Intensity vs excitation P_d log-log plots of different upconversion PL bands of $LiYbF_4$: x mol% $Ho^{3+}/LiYF_4$ RENPs under 960 nm laser excitation. Linear fits for the low P_d regime (2 – 20 W/cm^2), slope values are summarized in the table below.

Table S6. Slope values of linear fits in Figure S21.

Transition / x mol% Ho^{3+}	$^5F_3 \rightarrow {}^5I_8$	$^5S_2/^5F_4 \rightarrow {}^5I_8$	$^5F_5 \rightarrow {}^5I_8$	$^5S_2/^5F_4 \rightarrow {}^5I_7$
1	2.77 ± 0.24	2.23 ± 0.05	2.19 ± 0.05	2.14 ± 0.06
2	3.14 ± 0.13	2.42 ± 0.18	2.34 ± 0.17	2.89 ± 0.06
5	2.27 ± 0.11	2.49 ± 0.14	2.42 ± 0.19	2.86 ± 0.17

Decay and rise profiles of Ho^{3+}-RENPs excited states

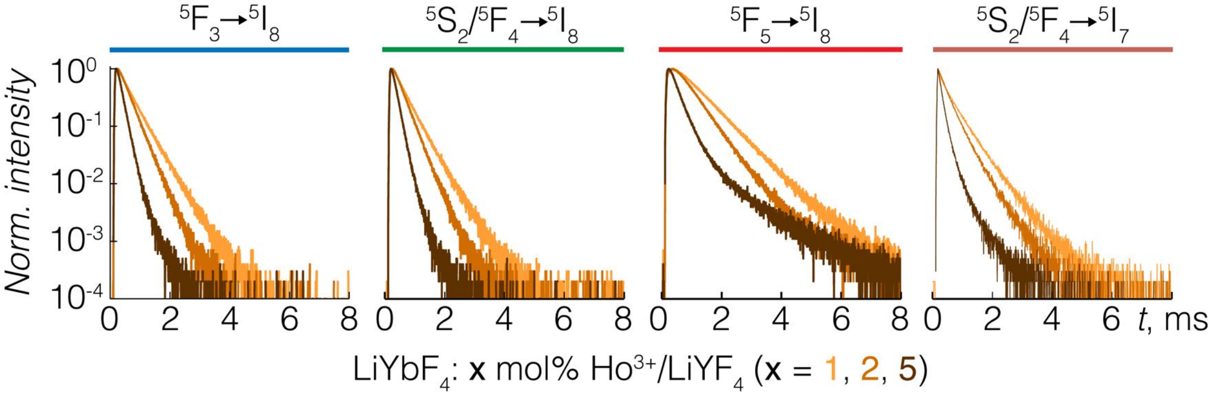

Figure S22. Normalized PL decay profiles of different upconversion emissions of LiYbF$_4$: x mol% Ho^{3+}/LiYF$_4$ RENPs under 980 nm laser excitation. Average decay values, τ, are summarized in Table S7.

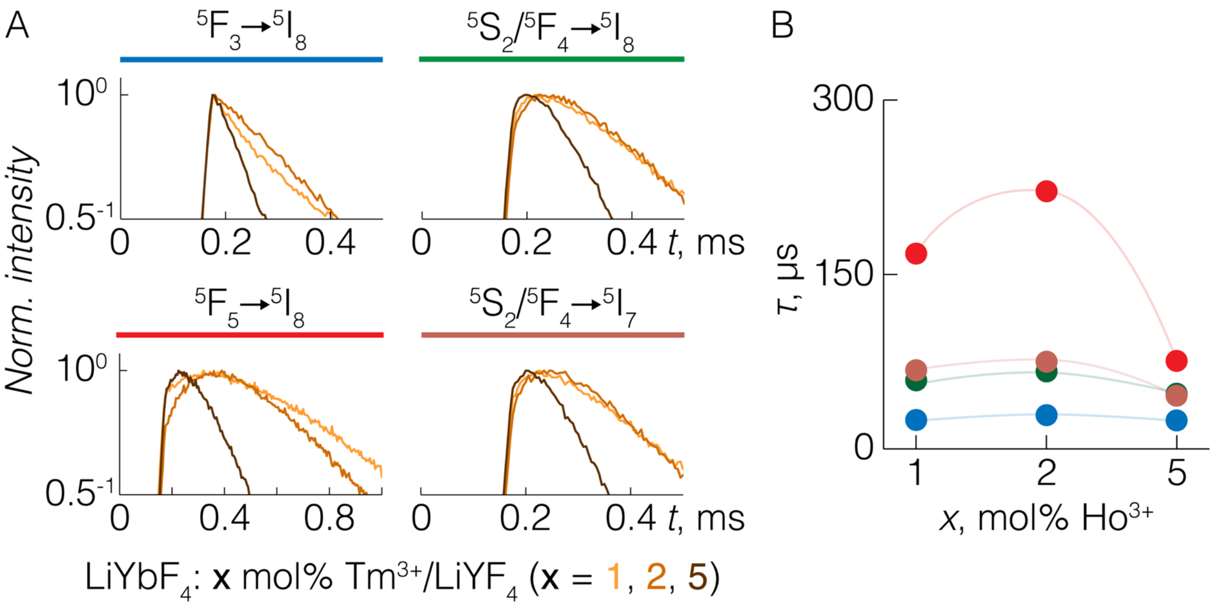

Figure S23. A – Close-up on the PL decay profiles in Figure S22, exemplifying change in the rise times with increasing Ho^{3+} doping concentration in LiYbF$_4$: x mol% Ho^{3+}/LiYF$_4$ RENPs. B - average rise time, τ_r, for different Ho^{3+} excited states as a function of Ho^{3+} concentration, also summarized in Table S5. Lines in B serve as guides to the eye.

Table S7. Average decay (τ) and rise (τ_r) times (in μs) of different Ho^{3+} excited states in $LiYbF_4$: x mol% $Ho^{3+}/LiYF_4$ RENPs. Values in parenthesis indicate relative change compared to the 1 mol% Ho^{3+} doping.

Transition / x mol% Ho^{3+}	$^5F_3 \rightarrow {}^5I_8$		$^5S_2/^5F_4 \rightarrow {}^5I_8$		$^5F_5 \rightarrow {}^5I_8$		$^5S_2/^5F_4 \rightarrow {}^5I_7$	
	τ	τ_r	τ	τ_r	τ	τ_r	τ	τ_r
1	410	25	486	59	1022	168	473	68
2	360 (-12%)	29 (+16%)	408 (-16%)	67 (+14%)	712 (-30%)	222 (+32%)	394 (-17%)	75 (+10%)
5	155 (-62%)	25 (0%)	212 (-56%)	84 (+42%)	398 (-61%)	76 (-55%)	208 (-56%)	46 (-32%)

UCQY of Ho^{3+}-RENPs

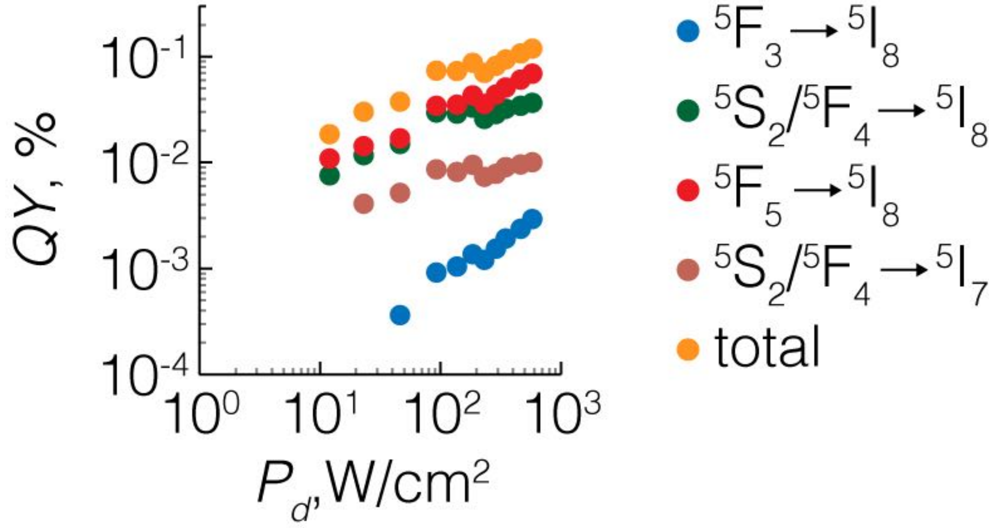

Figure S24. *UCQY* of LiYbF$_4$: 5 mol% Ho^{3+}/LiYF$_4$ RENPs vs 960 nm laser excitation P_d, measured for major Ho^{3+} upconversion PL bands.

Consideration for # of dopants and inter-ion distance

$LiYbF_4$ crystalizes into tetragonal ($I4_1/a$) crystal structure with $Z = 4$. Given unit cell parameters $a = b = 5.1335$ Å and $c = 10.588$ Å, the unit cell volume V_{cell} is ~0.279 nm^3. The morphology of $LiYbF_4$ RENPs can be approximated as a bipyramid with length and width equal to the measure of a minor axis (w), and height – major axis (h). In turn, volume (V_{RENPs}) of RENPs' core is expressed as:

$$V_{RENPs} = \frac{1}{3} w^2 h$$

Thus, the number of RE^{3+} dopants (#) per RENPs' core is:

$$\# = \frac{V_{RENPs}}{V_{cell}} \times Z \times c(RE^{3+})$$

Where, c(RE^{3+}) is fraction of activator dopant ions within a given RENPs' core.

The average inter-ion distance (d) can be expressed as:

$$d = \sqrt[3]{\frac{V_{cell}}{Z \times c(RE^{3+})}}$$

To illustrate change of energy transfer (ET) efficiency with inter-ion separation within the $LiYbF_4$ matrix, we simply considered the progression $1/R^n$ (n = 6, 8, 10), which respectively represents dipole-dipole (d-d), dipole-quadrupole (d-q), and quadrupole-quadrupole (q-q) interactions between the neighbouring ions.

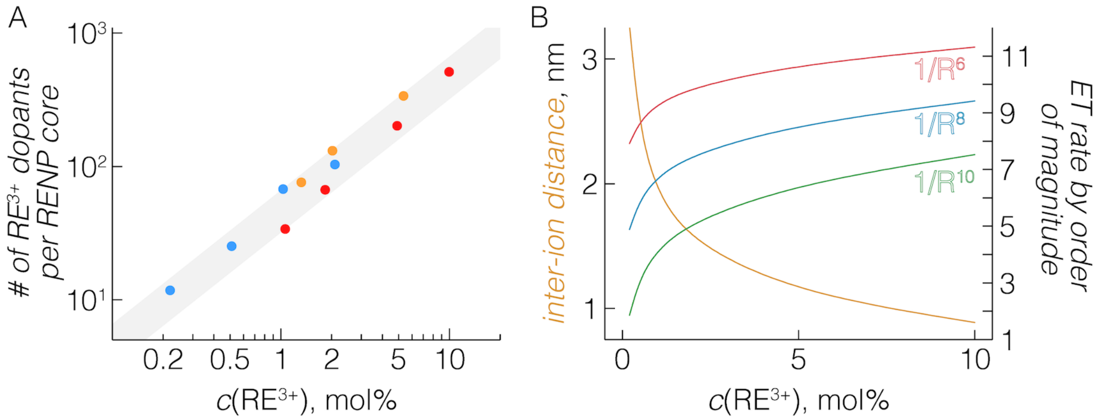

Figure S25. A – log-log plot of # of RE^{3+} activator ions per RENP core against mol% concentration of activator doping. Grey area indicates possible number of dopants for smallest and largest sized cores in our study. Coloured points represent estimates of # of RE^{3+} ions for each of the activator ion studied (blue – Tm^{3+}, red – Er^{3+}, and orange – Ho^{3+}) with respective core size and doping amount information gathered from TEM and ICP-OES analysis. B – visualization of inter-ion distance change vs mol% concentration of RE^{3+} doping in the $LiYbF_4$ matrix, as well as its influence, in measure of order of magnitude, on the inter-ion ET rates for d-d ($1/R^6$), d-q ($1/R^8$), and q-q ($1/R^{10}$) interactions.

CIE colour coordinates of $LiYbF_4$:RE^{3+}/$LiYF_4$ RENPs

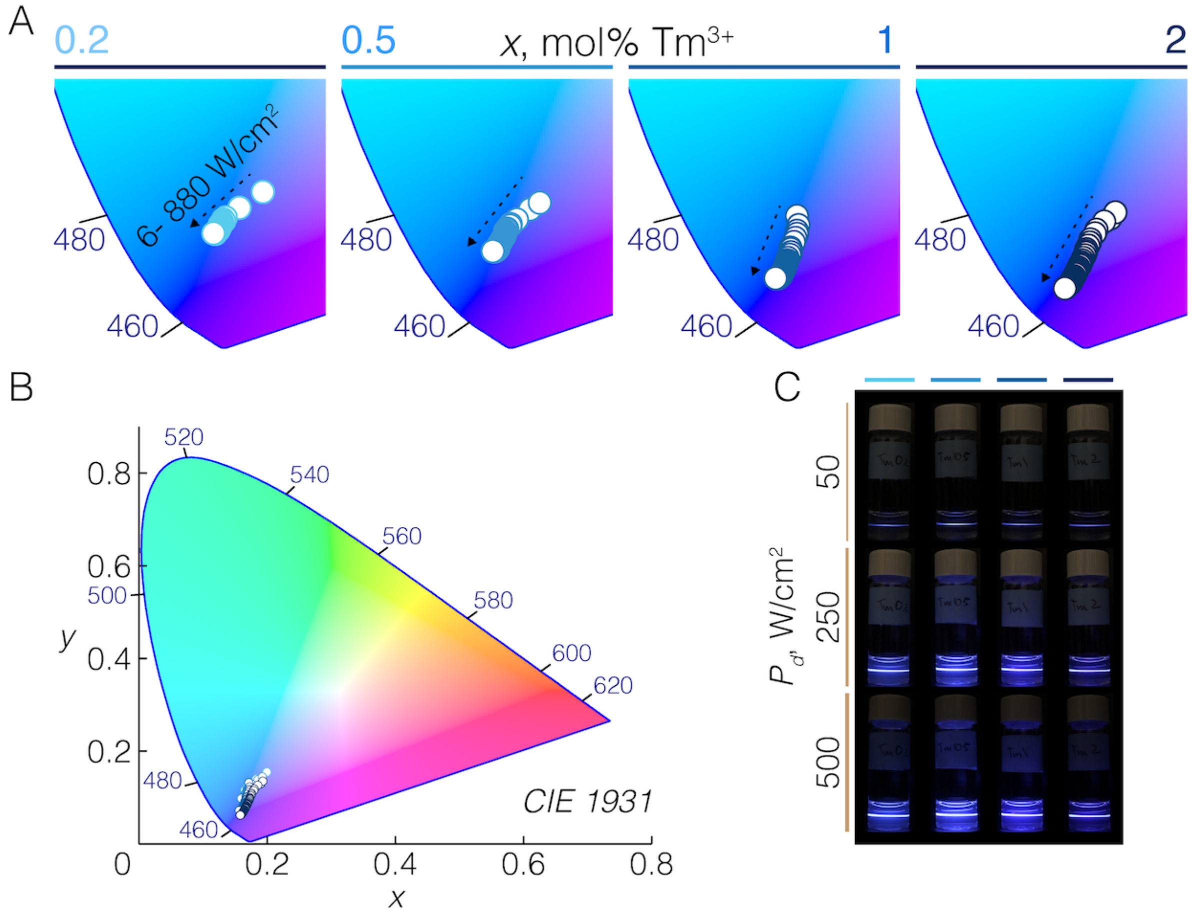

Figure S26. A, B – close-up and complete visualization of CIE colour coordinates for $LiYbF_4$: x mol% Tm^{3+}/$LiYF_4$ RENPs at different 960 nm laser excitation P_d. C – photographs of upconversion emission trace in hexane dispersions of $LiYbF_4$: x mol% Tm^{3+}/$LiYF_4$ RENPs under 960 nm laser excitation of different P_d.

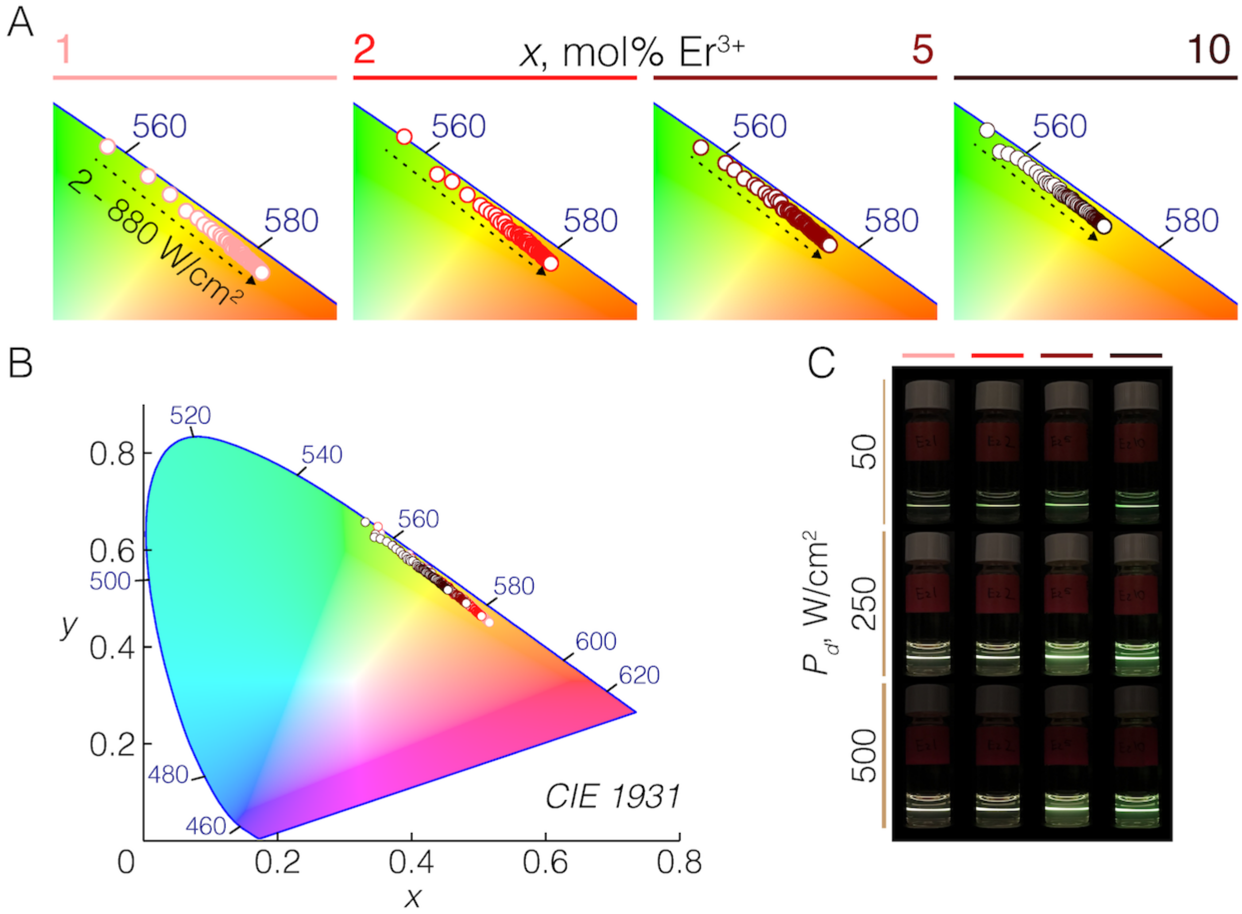

Figure S27. A, B – close-up and complete visualization of CIE colour coordinates for $LiYbF_4$: x mol% Er^{3+}/$LiYF_4$ RENPs at different 960 nm laser excitation P_d. C – photographs of upconversion emission trace in hexane dispersions of $LiYbF_4$: x mol% Er^{3+}/$LiYF_4$ RENPs under 960 nm laser excitation of different P_d.

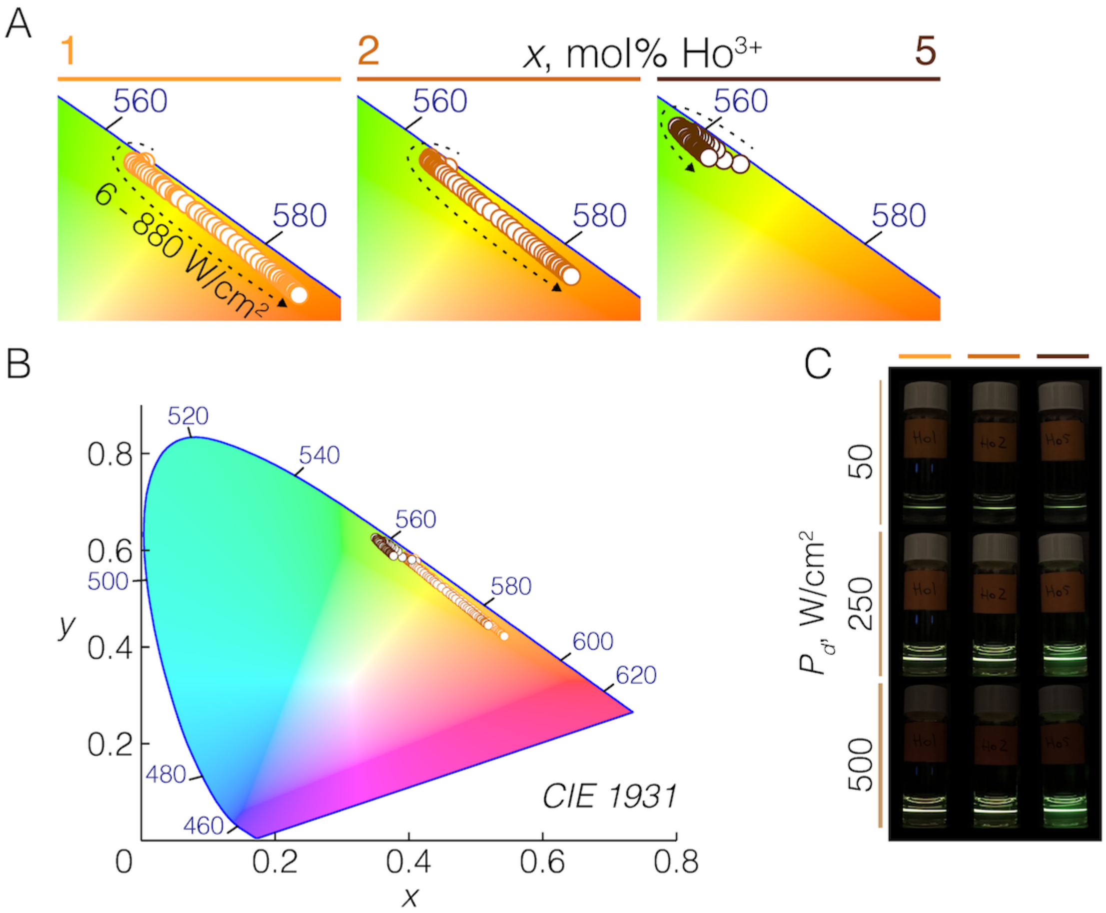

Figure S28. A, B – close-up and complete visualization of CIE colour coordinates for LiYbF$_4$: x mol% Ho^{3+}/LiYF$_4$ RENPs at different 960 nm laser excitation P_d. C – photographs of upconversion emission trace in hexane dispersions of LiYbF$_4$: x mol% Ho^{3+}/LiYF$_4$ RENPs under 960 nm laser excitation of different P_d.

Downshifting spectra of LiYbF$_4$:RE^{3+}/LiYF$_4$ RENPs

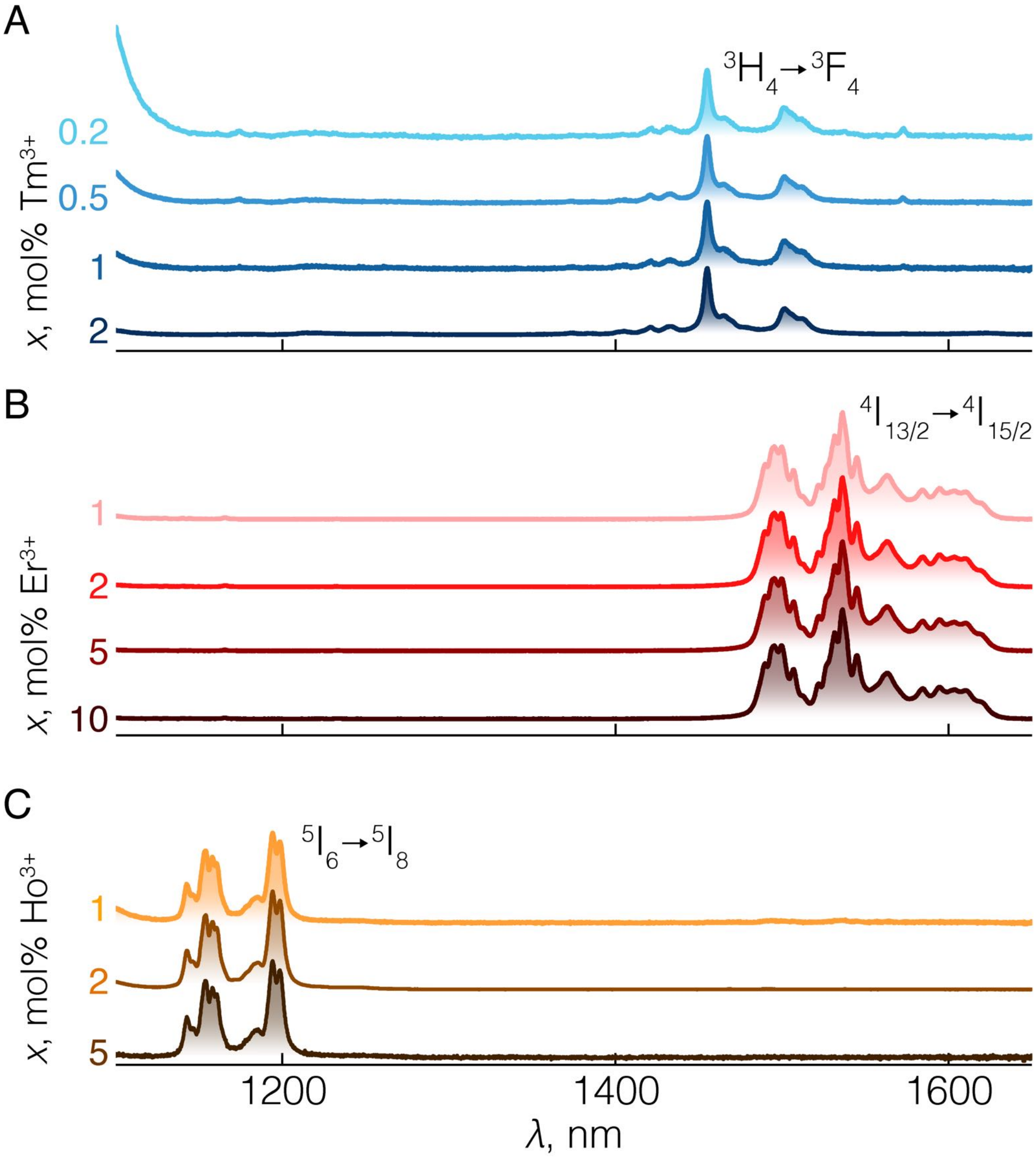

Figure S29. Normalized downshifting emission spectra of LiYbF$_4$: x mol% RE^{3+}/LiYF$_4$ RENPs under 960 nm excitation (~30 W/cm$_2$). A – Tm^{3+}, B – Er^{3+}, C – Ho^{3+}.

Tm^{3+}-RENPs – *UCQY* comparison

Table S8. *UCQY* comparison of different Tm^{3+}-doped RENPs. c/s – core/shell. For reference [2], two values are presented for similar power density as measured with different set-ups. For reference [3], values were extracted directly from provided *UCQY* plots, thus here are given as approximates.

Composition of RENPs	*Size*, nm	*UCQY*, % @ P_d, W/cm^2	REF
$LiYF_4$: 0.5 mol% Tm^{3+}, 25 mol% Yb^{3+}	89 x 50	0.016 ($^1D_2 \rightarrow {}^3F_4$) @ 40 0.00765 ($^1D_2 \rightarrow {}^3F_4$) @ 42	M. S. Meijer et al., (*Phys. Chem. Chem. Phys.* 2018)[2]
		0.025 ($^1G_4 \rightarrow {}^3H_6$) @ 40 0.0155 ($^1G_4 \rightarrow {}^3H_6$) @ 42	
		0.012 ($^1G_4 \rightarrow {}^3F_4$) @ 40 0.00799 ($^1G_4 \rightarrow {}^3F_4$) @ 42	
		3.4 ($^3H_4 \rightarrow {}^3H_6$) @ 40 2.56 ($^3H_4 \rightarrow {}^3H_6$) @ 42	
β-NaYF4: 0.5% mol% Tm^{3+}, 20 mol% Yb^{3+}	30.5 x 35.1	~0.025 (all transitions from $^1D_2$) @ 40	M. Kraft et al., (Methods Appl. Fluoresc. 2019)[3]
		~0.03 (all transitions from $^1G_4$) @ 40	
β-NaYF4: 1.2% mol% Tm^{3+}, 20 mol% Yb^{3+}	29.2 x 32.7	~ 6 ($^3H_4 \rightarrow {}^3H_6$) @ 40	
$LiYbF_4$: 0.5 mol% Tm^{3+}/$LiYF_4$	26.7 x 33.3	0.14 (UV, 330-400 nm) @ 100	W. Zheng et al., (*Nat. Comm.* 2018)[4]
		0.29 (blue, 430-530 nm) @ 100	
		0.05 (red, 630-700 nm) @ 100	
$LiLuF_4$: 0.5 mol% Tm^{3+}, 20 mol% Yb^{3+}/$LiLuF_4$	core – 28	0.61 (PL across 320-850 nm) @ 127	P. Huang et al., (*Angew. Chem. Int. Ed.* 2014)[5]
	c/s – 50	7.6 (PL across 320-850 nm) @ 127	
$LiYbF_4$: 1 mol% Tm^{3+}/$LiYF_4$	30	0.81 (PL across 330-840 nm) @ 70	Q. Zou et al., (*Nanoscale* 2017)[6]
$LiYbF_4$: 0.5 mol% Tm^{3+}/$LiYF_4$	26 x 25	0.0033 ($^1I_6 \rightarrow {}^3F_4$) @ 46	This work
$LiYbF_4$: 1 mol% Tm^{3+}/$LiYF_4$	28 x 25	0.0017 ($^1D_2 \rightarrow {}^3H_6$) @ 46	
		0.0063 ($^1D_2 \rightarrow {}^3F_4$) @ 46	
$LiYbF_4$: 0.5 mol% Tm^{3+}/$LiYF_4$	26 x 25	0.023 ($^1G_4 \rightarrow {}^3H_6$) @ 46	
		0.010 ($^1G_4 \rightarrow {}^3F_4$) @ 46	
$LiYbF_4$: 2 mol% Tm^{3+}/$LiYF_4$	25 x 24	1.22 ($^3H_4 \rightarrow {}^3H_6$) @ 46	

References

(1) Cheng, T.; Marin, R.; Skripka, A.; Vetrone, F. Small and Bright Lithium-Based Upconverting Nanoparticles. *J. Am. Chem. Soc.* **2018**, *140* (40), 12890–12899.

(2) Meijer, M. S.; Rojas-Gutierrez, P. A.; Busko, D.; Howard, I. A.; Frenzel, F.; Würth, C.; Resch-Genger, U.; Richards, B. S.; Turshatov, A.; Capobianco, J. A.; Bonnet, S. Absolute Upconversion Quantum Yields of Blue-Emitting $LiYF_4$:Yb^{3+},Tm^{3+} Upconverting Nanoparticles. *Phys. Chem. Chem. Phys.* **2018**, *20* (35), 22556–22562.

(3) Kraft, M.; Würth, C.; Palo, E.; Soukka, T.; Resch-Genger, U. Colour-Optimized Quantum Yields of Yb, Tm Co-Doped Upconversion Nanocrystals. *Methods Appl. Fluoresc.* **2019**, *7* (2), 024001.

(4) Zheng, W.; Huang, P.; Gong, Z.; Tu, D.; Xu, J.; Zou, Q.; Li, R.; You, W.; Bünzli, J.-C. G.; Chen, X. Near-Infrared-Triggered Photon Upconversion Tuning in All-Inorganic Cesium Lead Halide Perovskite Quantum Dots. *Nat. Commun.* **2018**, *9* (1), 3462.

(5) Huang, P.; Zheng, W.; Zhou, S.; Tu, D.; Chen, Z.; Zhu, H.; Li, R.; Ma, E.; Huang, M.; Chen, X. Lanthanide-Doped $LiLuF_4$ Upconversion Nanoprobes for the Detection of Disease Biomarkers. *Angew. Chem. Int. Ed.* **2014**, *53* (5), 1252–1257.

(6) Zou, Q.; Huang, P.; Zheng, W.; You, W.; Li, R.; Tu, D.; Xu, J.; Chen, X. Cooperative and Non-Cooperative Sensitization Upconversion in Lanthanide-Doped $LiYbF_4$ Nanoparticles. *Nanoscale* **2017**, *9* (19), 6521–6528.